Desalination and Water Treatment
www.deswater.com

36 (2011) 41–49
December

1944-3994/1944-3986
doi: 10.5004/dwt.2011.1831

Simulation of vacuum membrane distillation coupled with solar energy: Optimization of the geometric configuration of a helically coiled fiber

Adel Zrelli*, Béchir Chaouchi, Slimane Gabsi

Unité de Recherche Environnement Catalyse et Analyse des Procédés, Ecole Nationale d'Ingénieurs de Gabès, Université de Gabès, Rue Omar Ibn ElKhattab-6029 Gabès, Tunisie
Tel.: +75392100; fax: +75392190; email: Adel.Zrelli@yahoo.fr

Received 12 December 2009; accepted 28 February 2011

ABSTRACT

This work focuses on solar energy coupled with vacuum membrane distillation (VMD) for brackish water desalination. VMD is an evaporative process, using porous and hydrophobic membranes, permit to obtain the gaseous permeate, under vacuum, from the aqueous liquid feed. The aim of this work was to simulate the influence of operating conditions (feed flow, feed temperature) and hollow fibers membrane characteristics (pitch and curvature radius) on the permeate flow rate. The model formulation takes into consideration the variation of the physical characteristics of brackish solution and the water permeability of membrane. We used in this case a membrane module, composed of hollow fiber wound in helically coiled shape and placed in the absorber of the parabolic trough concentrator. Two dimensional Navier–Stokes equations were written and were solved with the finite element method. For the pitch of 32.2 mm and the coil radius of 95.7 mm, the simulation results of the permeate product are 0.2685 kg/h and 7.688 10^{-3} kg/s m^2 for the permeate flux.

Keywords: Desalination; Vacuum membrane desalination; Solar energy; Helical fiber

1. Introduction

Membrane distillation (MD) is a thermal process based on highly porous and hydrophobic membrane. It is a membrane technique for separating water vapor from brackish water by transport through the pores of membranes. The driving force of this process is the difference between vapor pressures created by temperatures difference across the membrane [1,2].

Moreover, MD has many desirable advantages compared to other distillation processes such as compactness, low energy consumption, possibility to use low temperature heat and perceivably immunity to fouling [3].

MD systems can be classified into four different configurations according to the nature of the cold side of the membrane [4]: The first configuration is the direct contact membrane distillation (DCMD) in which the membrane is in direct contact with liquid phases in both sides. The volatile components of the feed evaporate at the interface feed–membrane diffuse through the air filling up the membrane pores and condensate at the cold side in the distillate stream [5–7]. The second configuration is air gap membrane distillation (AGMD) in which an air gap is interposed between the membrane and the condensate surface. In this case, the air gap

*Corresponding author

functions as thermal insulation between membrane and condenser wall [8,9]. The sweeping gas membrane distillation (SGMD) represents the third configuration. In this configuration, a sweeping gas is used as carrier for the produced vapor. The condensation of this vapor is occurred out of the membrane [10]. The fourth and the last configuration is the vacuum membrane distillation (VMD), in which the vapor phase is vacuumed from the liquid through the membrane and condensed outside of the module [11–13]. This configuration combines two advantages which are a very low conductive heat loss and a reduced mass transfer resistance.

In order to enhance the permeate flux, VMD can be coupled with alternate source of energy like solar energy [14]. Different configurations can be used in order to couple VMD and solar energy. Also, membrane can be placed in or out the absorber of the solar collector.

A number of absorber configurations are used nowadays such as a flat plate, line-axis concentrating, or point focusing [15]. In this work, we are interested by the line-axis concentrating which offer the possibility to insert the membrane in the absorber and to obtain a maximum operation temperature in comparison to the flat plate [16].

According to the literature, and when the hollow fiber membrane has a helically coiled form, the permeate flux is enhanced [17–19]. In addition, we have a cross flow of the hot feed on the outside surface of hollow fiber membrane which allows to enhance of the outside heat transfer coefficient.

This work is composed of two parts. In the first part, we optimized the hollow fibers membrane characteristics such as the pitch and the curvature radius. In the second, we simulate the influence of operating conditions, which are the feed flow and feed temperature on the permeate flow rate.

2. Material and methods

2.1. Design description

The solar desalination installation shown in Fig. 1, is composed of parabolic trough concentrator. At the

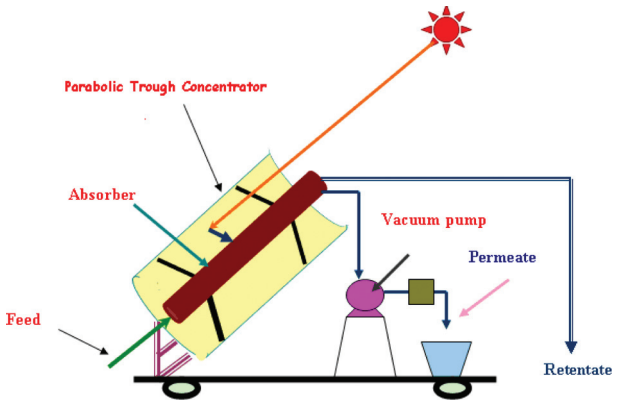

Fig. 1. Solar-VMD installation.

focal axis is mounted the absorber, which is in the shape of cylindrical tube. This absorber contains the hollow fibers membrane. This membrane has the shape of coil and the configuration of absorber and membrane is similar to a helically coiled heat exchanger. In addition to that, solar rays are focused into the absorber, and an increasing of the feed temperature is consequently reported.

In order to have a symmetrical conception, we study a system which contains two helically coiled fibers (Fig. 2). Since the flow is symmetric about a vertical plane passing through the axis of the cylinder, only the half-plane needs to be considered (Fig. 3).

2.2. Mathematical model

Based on Figs. 2 and 3, we developed a mathematical model and the following assumptions are used for the numerical calculations:

1. The flow is fully developed before it enters the inlet of the absorber [20].
2. Fluid is incompressible and Newtonian.
3. The motion is considered as axisymmetric, hence, only half of the absorber is considered.
4. The gravity force is neglected [20].

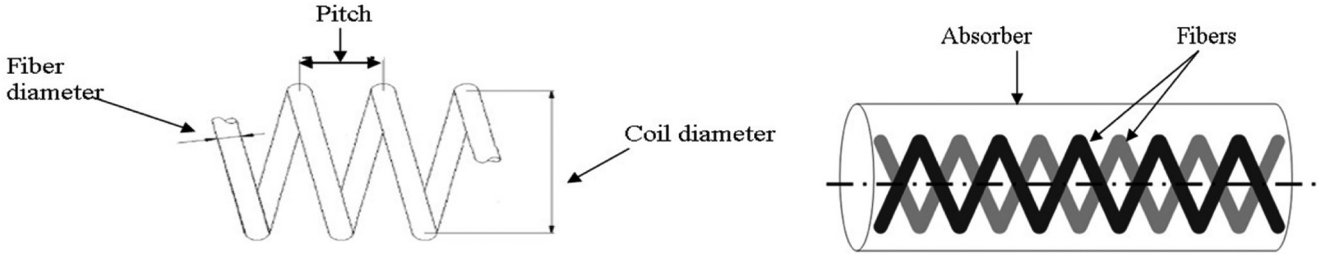

Fig. 2. Basic geometry of a helical fiber.

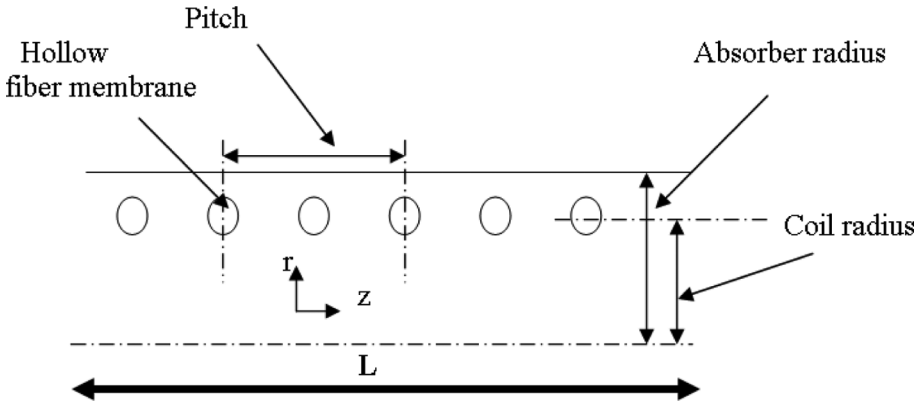

Fig. 3. Domain of study.

5. All angular gradients parameters are negligible; the model can be described in the coordinates r and z.
6. No slip condition is valid on the surface of fiber.

All simulations are carried out assuming steady state and a symmetric wake behind each fiber [20,21].

Under these conditions, the appropriate governing equations are written [22]:

$$\text{Continuity equation:} \quad \frac{\partial u_r}{\partial r} + \frac{u_r}{r} + \frac{\partial u_z}{\partial z} = 0, \tag{1}$$

$$\text{Momentum equations:} \; u_r \frac{\partial u_r}{\partial r} + u_z \frac{\partial u_z}{\partial z} = \nu \left[\frac{\partial}{\partial r} \left(\frac{1}{r} \frac{\partial r u_r}{\partial r} \right) + \frac{\partial^2 u_r}{\partial z^2} \right], \tag{2}$$

$$u_r \frac{\partial u_z}{\partial r} + u_z \frac{\partial u_z}{\partial z} = -\frac{1}{\rho} \frac{\partial P}{\partial z} + \nu \left[\frac{1}{r} \frac{\partial}{\partial r} \left(r \frac{\partial u_z}{\partial r} \right) + \frac{\partial^2 u_z}{\partial z^2} \right], \tag{3}$$

$$\text{Energy equation:} \; u_r \frac{\partial \mathrm{T}}{\partial r} + u_z \frac{\partial T}{\partial z} = \alpha \left[\frac{1}{r} \frac{\partial}{\partial r} \left(r \frac{\partial T}{\partial r} \right) + \frac{\partial^2 T}{\partial z^2} \right]. \tag{4}$$

The boundary conditions for velocity and temperature are:

At the inlet of absorber, $Z = 0$:

$$\begin{aligned} u_z &= 2u_0 \left(1 - \left(\frac{r}{R} \right)^2 \right) \\ u_r &= 0 \\ T &= T_{in} \end{aligned} \tag{5}$$

At the exit, $Z = L$:

$$u_r = \frac{\partial u_z}{\partial z} = \frac{\partial \mathrm{T}}{\partial z} = 0 \text{ [23]}. \tag{6}$$

At the hollow fiber membrane surface:

$$\begin{aligned} u_z &= 0 \\ u_r &= 0 \\ T &= T_{inter} \end{aligned} \tag{7}$$

At the absorber interior wall, r = R:

$$\begin{aligned} u_z &= 0 \\ u_r &= 0 \\ T &= T_{\mathrm{w}} \end{aligned} \tag{8}$$

The temperature at the feed–membrane interface (T_{inter}) is related to the bulk temperature (T_{b}) by the following heat balance equation [24]:

$$J_{\mathrm{v}} L_{\mathrm{v}} = h_{\mathrm{f}} (T_{\mathrm{b}} - T_{\mathrm{inter}}). \tag{9}$$

The latent heat of vaporization of water (L_{v}) is given by:

$$L_{\mathrm{v}} = 2538.2 - 2.91 T_{\mathrm{inter}} \text{[15]}. \tag{10}$$

The absorber interior wall temperature (T_{w}) is given by the below equation:

$$T_{\mathrm{w}} = T_{\mathrm{e}} - \frac{q_{\mathrm{u}} e}{\lambda_{\mathrm{m}}}, \tag{11}$$

where T_{e} is the absorber exterior wall temperature and q_{u} is the useful heat flow, given by:

$$q_{\mathrm{u}} = q_{\mathrm{a}} - q_{\mathrm{e}}. \tag{12}$$

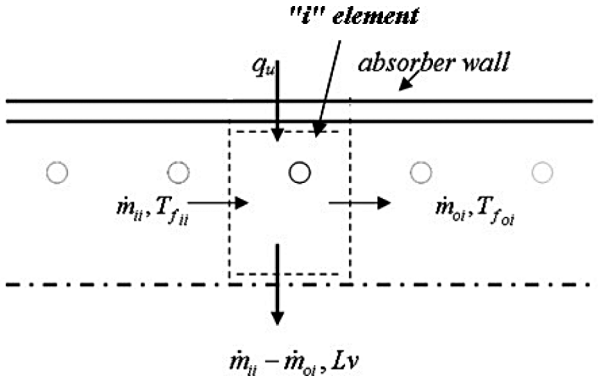

Fig. 4. Thermal balance on the ''i'' element of the absorber.

The incident power of the absorber radiance, ''q_a'', is expressed by:

$$q_a = IC_g\rho\gamma\alpha\tau. \tag{13}$$

The sum of the heat losses by convection and radiation between the absorber and the surrounding, ''q_e'', is given by:

$$q_e = \varepsilon_a\sigma(T_e^4 - (T_a - 11)^4) + (5.7 + 3.8w_s)(T_e - T_a). \tag{14}$$

The thermal energy balance equation of the absorber ''i'' element (Fig. 4) is:

$$q_u s_i = \dot{m}_{oi}cpT_{foi} - \dot{m}_{ii}cpT_{fii} + (\dot{m}_{ii} - \dot{m}_{oi})Lv \tag{15}$$

The dominant mechanism of mass transfer through the membrane pores at low vacuum pressures is Knudsen [14,25]. This model suggests a linear relationship between the permeate flux (J_v) and the transmembrane water vapor pressure difference ($\triangle P$) [26]:

$$J_v = \frac{k_m}{\sqrt{M_w}}\Delta P = \frac{k_m}{\sqrt{M_w}}(P_{inter} - P_v). \tag{16}$$

The membrane permeability coefficient (k_m) can be related to membrane structural properties such as its membrane thickness (δ), pore tortuosity (τ) and pore radius (r) [24]:

$$k_m = 1.064\frac{r\varepsilon}{\delta\tau}\sqrt{\frac{1}{RT}} \tag{17}$$

The water vapor pressure (P_{inter}) at the liquid–vapor interface may be related with the temperature, by using the Antoine's equation [27]:

$$P_{inter}(T) = \exp\left(23.238 - \frac{3841}{T - 45}\right), \tag{18}$$

where $P_{inter}(T)$ is in Pa and T is in K.

Following an analogy between the helically coiled fiber and the coiled tube heat exchanger, we used the correlation presented by Salimpour [28,29] in order to calculate the outside heat transfer coefficient.

Equation	Comments
$Nu = 19.64\mathrm{Re}^{0.513}\mathrm{Pr}^{0.129}\gamma^{0.938}$ (19)	$60 < \mathrm{Re} < 550, 0.058 < \gamma < 0.095$ $5 < \mathrm{Pr} < 7$ $\gamma = \frac{P}{2\pi R_c}$

The equations of temperature dependant properties, for water, are given by [30]:

$$\mu(T) = (-2.1897\mathrm{e} - 11)T^4 - (3.055\mathrm{e} - 8)T^3 + (1.6028\mathrm{e} - 5)T^2 - 0.0037524T + 0.33158, \tag{20}$$

$$\rho(T) = (-1.53629\mathrm{e} - 5)T^3 + 0.011778T^2 - 3.0726T + 1227.8, \tag{21}$$

$$k(T) = (1.5362\mathrm{e} - 8)T^3 - (2.261\mathrm{e} - 5)T^2 + 0.010879T - 1.0294, \tag{22}$$

$$cp(T) = (1.1105\mathrm{e} - 5)T^3 - 0.0031078T^2 - 1.478T + 4631.9. \tag{23}$$

The helically coil length (L_c) is given by:

$$L_c = \left(\frac{L + P}{P}\right)\sqrt{p^2 + (\pi Dc)^2} \tag{24}$$

For each ''i'' element of the absorber, we can calculate the permeate flow rate ''$\dot{m}_{pi}$'' according to the below equation:

$$\dot{m}_{pi} = J_{vi}\pi Lc_i d_o \tag{25}$$

2.3. Solution procedure

The partial differential equations for continuity, momentum and energy, Eqs. (1)–(4) are discretized

Table 1
Design specifications and operating characteristics of the helically membrane module

Property	Value
Length of the module (mm)	233
Module coil radius (mm)	195.2
Inner diameter of fiber (mm) [17]	0.27
outer diameter of fiber (mm) [17]	0.62
Pitch (mm)	25
Number of fibers	2
Inlet feed velocity (m/s)	3.4×10^{-4} ($Re = 68$)
Vacuum pressure (Pa)	1,000
Inlet feed temperature (°C)	20

by means of a finite element method. Since the temperature profiles are assumed to have no influence on the hydrodynamics, they are calculated after the velocity distributions are known. The iteration procedure for the solution of coupled equations of hydrodynamics and heat transfer is as following:

- The velocity profile and the temperature in the inlet of the absorber are specified.
- For the calculation of the temperature and velocity distributions, all the membrane interfaces temperatures and the elementary external wall absorber temperatures were guessed.
- The absorber interior wall temperature (T_w) is determined by resolving the system of equations (11)–(14).
- Solve energy equation, Eq. (4), at the boundary conditions, Eqs. (5)–(8), to obtain the bulk temperature for the first element of fiber.
- The membrane interface temperature for the first element fiber is determined by resolving the nonlinear system of equations (9)–(10), (16)–(19).
- The resulting temperature was compared to the guessed value. In case the difference was greater than the tolerance limit ($3 \times 10^{-3}\%$), a new guess for the membrane interface temperature was applied, being the calculated value. When the difference between the two temperature values was within the prescribed limit, the corresponding temperature was taken as a boundary condition. So the permeate flux, of the fiber element number ''1'' (J_v1) is determined also the permeate flow rate '' $\dot{m}_{p1}$''. If the difference between ''$\dot{m}_{p1}$'' and the value of ''$\dot{m}_{i1} - \dot{m}_{o1}$'', given by Eq. (15), was greater than the tolerance limit (0.2%), a new guess for the elementary external wall temperature was applied. When the difference between the two values of the flow rates was within the prescribed limit, the permeate flow rate is determined. This procedure is then repeated for all elements of the absorber.

Table 2
Geometrical and optical parameters of the absorber

Absorber configuration	Parameters
Length of the absorber (m)	0.233
Inside diameter of the absorber (mm)	206.5
Outside diameter of the absorber (mm)	219.1
Absorptivity of the absorber	0.9
Reflectivity of the absorber	0.9
Transmissivity	1
Intercept factor	0.9
Emissivity of absorber	0.9

All these steps were carried out on a PC with a CPU T 5200 1.6 GHz processor running under Windows XP pack3. The computed results were done using MATLAB and FemLab.

The mesh characteristics depend on the geometrical configuration of the helically coiled fiber. For example, when the values of the coil radius and the pitch were 0.095 and 3.22 m respectively, the grid presents 1,180 nodes.

3. Results and discussion

In order to optimize the geometric characteristics of the helically hollow fibers coil membrane, we simulate in the first, the variation of the permeate flow rate with the coil pitch. The summary of the inlet parameters are given in Tables 1 and 2.

The permeate flow rate variations with different pitches are shown in Fig. 5. From this figure, it can be seen that from the pitch value = 25 mm, the permeate flow rate increase to reach their maximum toward the pitch value = 32.2 mm and decrease thereafter.

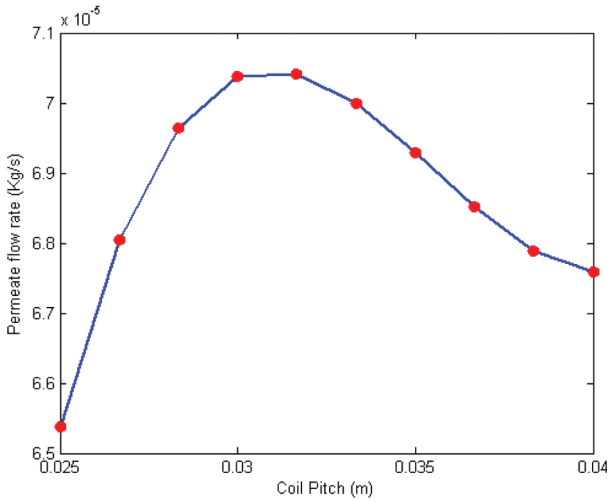

Fig. 5. Permeate flow rate as function of pitch.

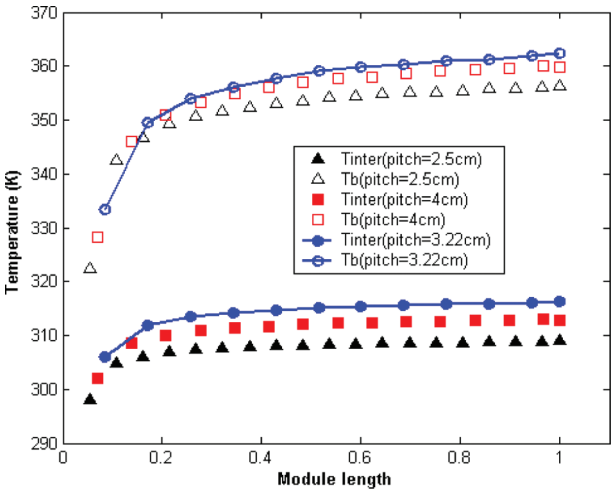

Fig. 6. Bulk and interface temperatures vs. module length for different pitches.

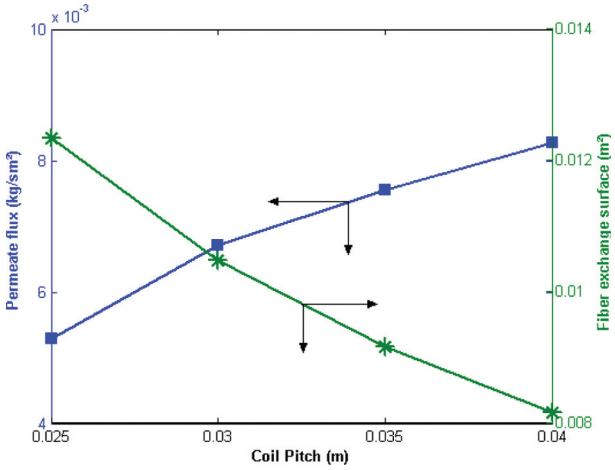

Fig. 8. Fiber exchange surface and permeate flux vs. coil pitch.

In order to explain this evolution, of the permeate flow rate, we plot in Fig. 6 the variations of the bulk and interface temperatures along the hollow fiber module and for three different pitches (2.5, 3.22 and 4 cm). Also, we plot in Fig. 7 the variations of the temperature polarization coefficient (T_{inter}/T_b) for these three pitches.

According to these figures, we can conclude that when the pitch decreases, the size of the wake also decreases, the empty space between the fibers available for bulk flow is deceased. This implies a decrease of velocity of feed and the Reynolds number, which causes the boundary layer heat transfer coefficient and the permeate flux to decrease. Also, when the pitch decreases, the fiber exchange surface increases (Fig. 8). These two variations of fiber exchange surface and the permeate flux lead to obtain the optimum pitch which is 32.2 mm.

Using the determined value of pitch, the optimum coil radius is obtained by simulation. The results are shown in Fig. 9. This figure illustrates the dependence of the permeate flow rate on the coil radius. As seen, it increases sharply to reach their maximum toward the coil radius value = 95.7 mm and decrease thereafter. Important to say that this decrease is due to the decrease of velocity which is influenced by the width of the channel between the outside face of fiber and the absorber interior wall. When the value of this width decrease, the effect of channel blockage is remarked [31]. Also, the parabolic profile of the inlet velocity, lead to obtain decreased values of velocity nears the absorber interior wall.

Fig. 10 shows the evolution of the simulated values of the permeate flow rate as function of the feed flow

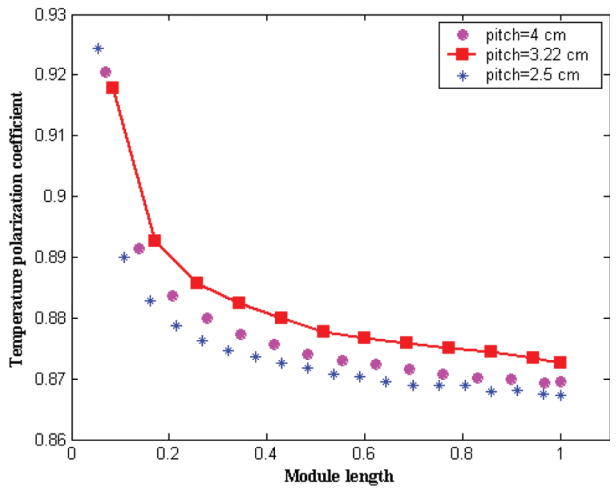

Fig. 7. Effects of pitch variation on temperature polarization coefficient.

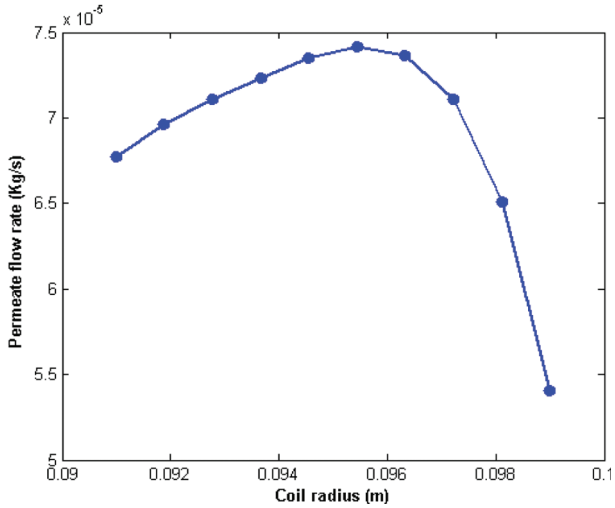

Fig. 9. Variation of permeate flow rate as function of coil radius.

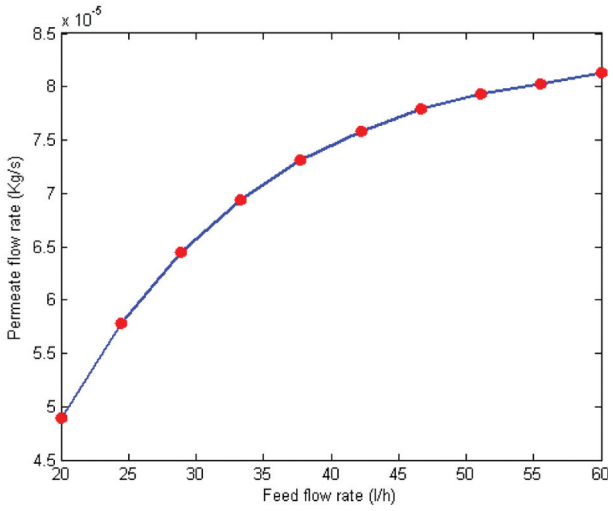

Fig. 10. Influence of feed flow rate on average permeate flow rate.

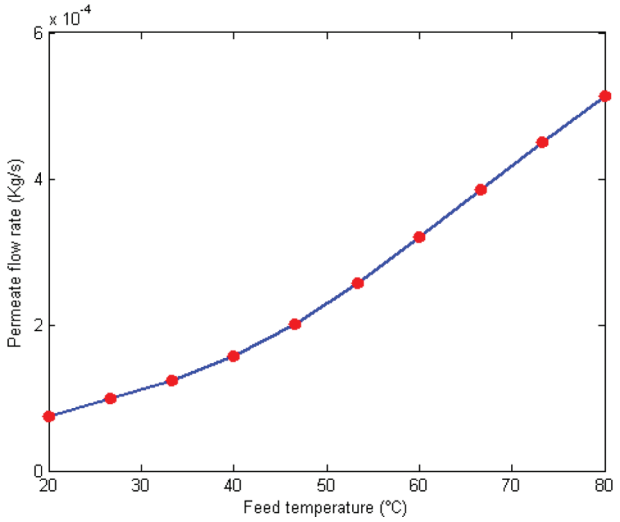

Fig. 11. Influence of feed temperature on the permeate flow rate.

rate. In this case, the permeate flow rate increases with the feed flow rate. This trend has been reported previously for various MD processes [8,27,32,33]. The relation between the permeate flow rate and the feed flow rate confirms the boundary layers presence in the feed side. The increase of feed velocity, and consequently the Reynolds number, causes an increase in the boundary layer heat transfer coefficient and the permeate flow rate.

It is important to remark that for the solar membrane distillation processes, the amount of energy collected is almost unchangeable for a specific operating day. For this reason, we may say that it is the reduced flow rate that allows the MD process to be operated at higher feed temperatures.

Relative to the feed flow rate, feed temperature has a small effect on the Reynolds number at a given feed flow rate. The small changes are only limited in the density and viscosity of feed. Although the increase of temperature enhances the Reynolds number somewhat, it enhances exponentially the permeate flow rate (Fig. 11). This effect can be attributed to the higher water vapor sensitivity at high temperatures (Eq. (18)). This causes the increase of vapor pressure difference or driving force ($P_{\text{inter}} - P_{\text{v}}$).

4. Conclusions

In this study, we are interested by the simulation of VMD coupled with solar energy. In this case, the membrane module used is composed of hollow fiber wound in helically coiled shape and placed in the absorber of the parabolic trough concentrator.

A mathematical system of equations using two-dimensional convective heat equations in cylindrical coordinate is developed. A numerical method, using a finite element method, for the solution of the resulting system of equations was developed in order to optimize the pitch and the radius of curvature of a helically hollow fibers coil membrane. The optimized coil radius and pitch for this solar installation configuration are 95.7 and 32.2 mm. In this case and in our operating conditions the obtained permeate flow rate is 0.2685 kg/h. Also, the simulation of the influence of operating conditions, which are the feed flow and the feed temperature, were presented.

Symbols

C_{g}	geometric concentration
Cp	specific heat capacity, J/kg K
D	Diameter, m
D_{c}	coil diameter, m
E	thickness of the wall absorber, m
h_{f}	boundary layer heat transfer coefficient of feed, W/m^2K
I	incident radiation on the level of the concentrator, W/m^2
J_{v}	permeate flux, kg/sm^2
k	thermal conductivity, W/m k
k_{m}	membrane permeability coefficient, s $mole^{1/2}$ m^{-1} $kg^{-1/2}$
L	module length, m
Lc	length coil, m
L_{v}	latent heat of vaporization, J/kg
$\dot{m}_{ii}$	feed flow rate in the inlet of element ‘‘i ’’, kg/s
$\dot{m}_{pi}$	permeate flow rate, kg/s

$\dot{m}_{oi}$	feed flow rate in the outlet of element ''i '', kg/s
M_w	water molar mass, kg/mol
P	pressure, Pa/Pitch, m
P_{inter}	water partial pressure in the membrane surface, Pa
P_v	vacuum pressure, Pa
q_a	incident power of the absorber radiance, W/m^2
q_e	heat flow loss, W/m^2
q_u	useful heat flow, W/m^2
r	radial coordinate
R	absorber radius, m
Rc	coil radius, m
s_i	outer side surface of the element ''i'' of the absorber, m^2
T	temperature, K
u_0	inlet average axial velocity, m/s
u_r	radial velocity, m/s
u_z	axial velocity, m/s
w_s	wind velocity, m/s
z	axial coordinate

Greek

α	absorption coefficient of absorber/ Thermal diffusivity, m^2/s
ε	emissivity of the absorber
γ	interception coefficient of absorber/ Dimensionless pitch
λ_m	thermal conductivity of the absorber enlightened face, W/mK
μ	dynamic viscosity, Kg/ms
ν	kinematic fluid viscosity, m^2/s
ρ	reflectivity coefficient/ Fluid density, Kg/m^3
σ	Stefan-Boltzmann constant, W/m^{2}K^4
τ	transmission coefficient of absorber

Subscript

a	ambient
b	bulk
e	absorber external wall
fii	fluid at the entrance of the element ''i'' of the absorber
foi	fluid at the exit of the element ''i'' of the absorber
in	inlet
inter	interface membrane/feed
o	out
w	wall

References

[1] C. Fernandez-Pineda, M. Izquierdo, and M.C. Garcia-Payo, Gas permeation and direct contact membrane distillation experiments and their analysis using different models, J. Membr. Sci., 198 (2002) 33-49.

[2] F. Lagana, G. Barbieri and E. Drioli, Direct contact membrane distillation: modelling and concentration experiments, J. Membr. Sci., 166 (2000) 1–11.

[3] A.M. Alklaibi and N. Lior, Membrane-distillation desalination: status and potential, Desalination, 171 (2004) 111–131.

[4] C.A. Rivier, M.C. Garcia-Payo, I.W. Marison and U. Von Syocar, Separation of binary mixtures by thermostatic sweeping gas membrane distillation. I. Theory and simulation, J. Membr. Sci., 201 (2002) 1–16.

[5] A.O. Imdakm and T. Matsuura, Simulation of heat and mass transfer in direct contact membrane distillation (MD): The effect of membrane physical properties, J. Membr. Sci., 262 (2005) 117–128.

[6] L. Martinez, Comparison of membrane distillation performance using different feeds, Desalination, 168 (2004) 359–365.

[7] Yanbin Yun, Runyu Ma, Wenzhen Zhang, A.G., Fane and Jiding Li, Direct contact membrane distillation mechanism for high concentration NaCl solutions, Desalination, 188 (2006) 251–262.

[8] C.M. Guijt, G.W. Meindersma, T. Reith and A.B. De Haan, Air gap membrane distillation. 2. Model validation and hollow fibre module performance analysis, Sep. Purif. Technol., 43 (2005) 245–255.

[9] R. Chouikh, S. Bouguecha and M. Dhahbi, Modelling of a modified air gap distillation membrane for the desalination of seawater, Desalination, 181 (2005) 257–265.

[10] M. Khayet, M.P. Godino and J.I. Mengual, Theoretical and experimental studies on desalination using the sweeping gas membrane distillation method, Desalination, 157 (2003) 297–305.

[11] F. Banat, S. Al-asheh and M. Qtaishat, Treatment of waters colored with methylene blue dye by vacuum membrane distillation, Desalination, 174 (2005) 87–96.

[12] T. Mohammadi and M. Akbarabadi, Separation of ethylene glycol solution by vacuum membrane distillation (VMD), Desalination, 181 (2005) 35–41.

[13] S. Bandini and G.C. Sarti, Concentration of must through vacuum membrane distillation, Desalination, 149 (2002) 253–259.

[14] D. Wirth and C. Cabassud, Water desalination using membrane distillation: comparison between inside/out and outside/ in permeation, Desalination, 147 (2002) 139–145.

[15] Béchir Chaouchi, Adel Zrelli and Slimane Gabsi, Desalination of brackish water by means of a parabolic solar concentrator, Desalination, 217 (2007) 118–126.

[16] L. Garcia-Rodroguez, A.I. Palmero-Marrero and C. Gomez-Camacho, Comparison of solar thermal technologies for applications in seawater desalination, Desalination, 142 (2002) 135–142.

[17] Hanuman Mallubhota, Sven Hoffman, Meike Schidt, Johan Vente and Georges Belfort, Flux enhancement during dean vortex tubular membrane nanofiltration. 10. Design,construction, and system characterization, J. Membr. Sci., 141 (1998), 183–195.

[18] Kenichi Nagase, Fukashi Kohori, Kiyotaka Sakai and Hiroyuki Nishide, Rearrangement of hollow fibers for enhancing oxygen transfer in an artificial gill using oxygen carrier solution, J. Membr. Sci., 254 (2005), 207–217.

[19] S.H. Liu, G.S. Luo, Y. Wang and Y.J. Wang, Preparation of coiled hollow-fiber membrane and mass transfer performance in membrane extraction, J. Membr. Sci. 215 (2003) 203–211.

[20] T. Li, N.G. Deen and J.A. Kuipers, Numerical investigation of hydrodynamics and mass transfer for in-line fiber arrays in laminar cross-flow at low Reynolds numbers, Chem. Eng. Sci., 60 (2005) 1837–1847.

[21] T. Kfinite Gowda, B.S.V. Patnaik and P.A. Aswatha Narayana, Finite element simulation of transient laminar flow and heat

transfer past in-line tube bank, Int. J. Heat and Fluid Flow, 19 (1998) 49–55.
[22] R. Byron Bird, Warren E. Stewart and Edwin N. Lightfoot, Transport Phenomena, 2nd ed., John Wiley & Sons, Inc., New York, 2002.
[23] R. Chouikh, A. Guizani and M. Maalej, A numerical study of the laminar natural convection flow around an array of two horizontal isothermal cylinders, Int. Comm. Heat Mass Transfer, 26 (3) (1999) 329–338.
[24] J.I. Mengual, M. Khayet and M.P. Godino, Heat and mass transfer in vacuum membrane distillation, Int. J. Heat Mass Transfer, 47 (2004) 865–875.
[25] M.A. Izquierdo and G. Jonsson, Factors affecting flux and ethanol separation performance in vacuum membrane distillation (VMD), J. Membr. Sci., 214 (2003) 113–130.
[26] C. Cabassud and D. Wirth, Membrane distillation for water desalination: how to chose an appropriate membrane? Desalination, 157 (2003) 307–314.
[27] F. Banat, R. Jumah and M. Garaibeh, Exploitation of solar energy collected by solar stills for desalination by membrane distillation, Renewable Energy, 25 (2002) 293–305.
[28] M.R. Salimpour, Heat transfer characteristics of a temperature-dependent-property fluid in shell and coiled tube heat exchangers, Int. Commun. Heat Mass Transfer, 35 (2008) 1190–1195.
[29] M.R. Salimpour, Heat transfer coefficients of shell and coiled tube heat exchangers, Exp. Thermal Fluid Sci., 33 (2009) 203–207.
[30] J.S. Jayakumar, S.M. Mahajani, J.C. Mandal, P.K. Vijayan and Rohidas Bhoi, Experimental and CFD estimation of heat transfer in helically coiled heat exchanger, Chem. Eng. Res. Design, 86 (2008) 221–232.
[31] E. Buyruk, Numerical study of heat transfer characteristics on tandem cylinders, inline and staggered tube banks in cross-flow of air, Int. Comm. Heat Mass Transfer, 29 (3) (2002), 355–366.
[32] Z. Ding, L. Liu, M.S. El-Bourawi and R. Ma, Analysis of a solar-powered membrane distillation system, Desalination, 172 (2005) 27–32.
[33] M. Gryta and M. Tomaszewka, Heat transport in the membrane distillation process, J. Membr. Sci., 144 (1998) 211–222.